Reducing Non-Radiative Voltage Losses by Methylation of Push–Pull Molecular Donors in Organic Solar Cells

Lukasz Baisinger,*[a] José María Andrés Castán,[b] Pablo Simón Marqués,[b] Giacomo Londi,[c] Clemens Göhler,[d] Carsten Deibel,[d] David Beljonne,[c] Clément Cabanetos,[b] Philippe Blanchard,[b] Johannes Benduhn,[a] Donato Spoltore,[a] and Karl Leo*[a]

Organic solar cells are approaching power conversion efficiencies of other thin-film technologies. However, in order to become truly market competitive, the still substantial voltage losses need to be reduced. Here, the synthesis and characterization of four novel arylamine-based push-pull molecular donors was described, two of them exhibiting a methyl group at the *para*-position of the external phenyl ring of the arylamine block. Assessing the charge-transfer state properties and the effects of methylation on the open-circuit voltage of the device showed that devices based on methylated versions of the molecular donors exhibited reduced voltage losses due to decreased non-radiative recombination. Modelling suggested that methylation resulted in a tighter interaction between donor and acceptor molecules, turning into a larger oscillator strength to the charge-transfer states, thereby ensuing reduced non-radiative decay rates.

Introduction

Over the past few years, organic solar cells (OSCs) have seen a rapid increase in their performance, approaching other thin-film technologies: Recent progress in the development of non-fullerene acceptors (NFAs) allowed to push the power conversion efficiencies (PCEs) above 18 %.[1] While the best-performing OSCs now have external quantum efficiency (EQE) and fill factor (FF) values both exceeding 80 %,[2,3] the open-circuit voltage (V_{oc}) is still lagging behind other thin-film technologies. Even in cases where the optical gaps are comparable, the substantial contribution of non-radiative losses in devices based on organic molecules limits the performances of organic photovoltaic devices (OPV).[3–5] Therefore, to further increase PCEs and thus market competitiveness of OSCs, the nature of those non-radiative voltage losses needs to be thoroughly understood.

Overall, the V_{oc} of OSCs is dictated by several factors: the optical gap (E_g^{opt}) of the light-absorbing materials, the energy of the intermolecular charge-transfer (CT) state at the donor-acceptor interface (E_{CT}), radiative voltage losses from the CT state (ΔV_r), and non-radiative voltage losses (ΔV_{nr}). The relation between those factors and the V_{oc} of the device can be expressed as Equation (1):[6–8]

$$qV_{oc} = E_g^{opt} - \Delta E_{CT} - k_B T \ln\left(\frac{k_{rad} N_{CTC}}{G_{CT}}\right) - k_B T \ln\left(\frac{1}{EQE_{EL}}\right) \quad (1)$$

where q is the elementary charge, k_B the Boltzmann constant, T the temperature, N_{CTC} the density of CT states, G_{CT} the generation rate, and EQE_{EL} the external electroluminescence (EL) quantum efficiency. According to the assumptions of the detailed balance theory and reciprocity relation between emission and absorption, this formula connects the electrical properties of the V_{oc} to the molecular CT state parameters. At 0 K the V_{oc} of the device is limited by E_{CT}, while at higher temperatures additional radiative and non-radiative recombination, represented by the two logarithms in Equation (1), further reduce the maximum achievable V_{oc}. The term ΔE_{CT} on the right-hand side of the Equation (1) is the energy required to convert photogenerated, strongly bound electron-hole pairs (excitons) into CT states and is therefore an energy loss mechanism. The energy difference between the lowest excited singlet state of either the donor (D) or the acceptor (A) and their corresponding CT state is referred to as driving force. For a long time, it was believed that a sizable driving force is necessary to achieve efficient exciton splitting and thus a good device performance. Recent studies point to the contrary, where

[a] L. Baisinger, Dr. J. Benduhn, Dr. D. Spoltore, Prof. Dr. K. Leo
Dresden Integrated Center for Applied Physics and Photonic Materials (IAPP) and Institute for Applied Physics
Technische Universität Dresden
Nöthnitzer Str. 61, 01187 Dresden (Germany)
E-mail: lukasz.baisinger@tu-dresden.de
          karl.leo@tu-dresden.de
[b] Dr. J. M. Andrés Castán, Dr. P. Simón Marqués, Dr. C. Cabanetos, Dr. P. Blanchard
UNIV Angers, CNRS, MOLTECH-Anjou, SFR MATRIX
2 bd Lavoisier, 49045 ANGERS Cedex (France)
[c] Dr. G. Londi, Prof. Dr. D. Beljonne
Laboratory for Chemistry of Novel Materials
University of Mons
Place du Parc, 20, 7000 Mons (Belgium)
[d] C. Göhler, Prof. Dr. C. Deibel
Institut für Physik
Technische Universität Chemnitz
Reichenhainer Str. 70, 09126 Chemnitz (Germany)

ChemSusChem

Full Papers
doi.org/10.1002/cssc.202100799

**Chemistry
Europe**

European Chemical
Societies Publishing

efficient charge carrier separation is characterized by a high internal quantum efficiency (IQE) and FF, even when the driving force is reduced below 10 meV.[9–11]

Following the detailed balance theory introduced by Shockley and Queisser, the V_{oc} of an ideal solar cell depends on the light intensity, the bandgap of the semiconductor, and temperature of the device.[12] In an ideal scenario, the EQE of the device is a step-function where the EQE of photons with energies above the band-gap is equal to unity. All recombination events in the device are occurring radiatively from the lowest excited state to the ground state, and the emission spectrum is equal to the product of black-body spectrum and absorption. In a real device, the edge of the EQE spectrum is instead broadened due to the nature of the transitions in organic semiconductors and additional absorption of the CT state, which further increases ΔV_r, leading to the radiative limit for the open-circuit voltage V_{rad} [Eq. (2)]:

$$V_{rad} = \frac{k_B T}{q} \ln\left(\frac{J_{sc}^{rad}}{J_0^{rad}} + 1\right) \tag{2}$$

where J_{sc}^{rad} is the short-circuit current density calculated from the integrated product of the EQE and AM1.5g spectra and J_0^{rad} is the upper radiative limit of the dark current obtained by integrating product of the EQE and black-body spectra. Radiative recombination is the reverse process to absorption and is thus an unavoidable, fundamental loss channel;[13] it is however possible to minimize those losses, for example by reducing the interface between donor and acceptor molecules[14] or by carefully selecting materials with reduced electron-phonon coupling or improved exciton dissociation.[15]

The V_{oc} of the real device is always lower than the radiative limit due to non-radiative voltage losses, often being the dominant non-geminate recombination process, and is directly related to the radiative efficiency EQE_{EL} [Eq. (3)]:[8]

$$\Delta V_{nr} = \frac{k_B T}{q} \ln\left(\frac{1}{EQE_{EL}}\right) = \frac{k_B T}{q} \ln\left(\frac{k_r + k_{nr}}{k_r}\right) \tag{3}$$

where k_r and k_{nr} are the radiative and non-radiative recombination rates, respectively. Previous studies have shown that this process is inherent to organic molecules, inversely proportional to the cell's effective gap (E_{CT}) and mediated by carbon-carbon vibrations.[16] Despite the observation of a clear trend following the so-called energy gap law, certain devices show significant deviations, even when E_{CT} is constant. These deviations from the energy gap law could be explained by taking into account additional parameters of the CT state, such as the oscillator strength f of the electronic transition or reorganization energy λ.[16,17] In this study. we investigate the influence of those molecular parameters on the performance of OSCs. For this purpose, we use a molecular system allowing a systematic variation of CT state properties.

Vacuum-processed OSCs based on well-defined small conjugated molecules constitute an excellent system to study structure-properties relationships.[18,19] In this context, small push-pull D-π-A molecules where an electron-donating block is connected to an electron-accepting group through a π-conjugated spacer have been widely investigated as promising donor materials in OPV.[20–25] For example, high-efficiency vacuum-processed OSCs using 2-[(7-(4-[N,N-bis(4-methylphenyl)amino]phenyl)- 2,1,3-benzothia-diazol-4-yl)methylene]-propane-dinitrile (DCDCPB) and its thiophenic analogue 2-((7-(5-(dip-tolylamino)thiophen-2- yl)benzo[c][1,2,5]thiadiazol-4-yl)-methylene (DTDCTB) donors were reported, showing exceptionally long exciton diffusion lengths (see the Supporting Information, Figure S1).[26–28] In these push-pull molecules, a benzothiadiazole (BTZ) π-spacer connects the dicyanovinyl (DCV) electron-acceptor block to two different arylamine-based donor blocks exhibiting two methyl groups at the *para*-positions of the two external phenyl rings. As shown by Chen et al., the presence of methyl groups leads to lower oxidation potentials, higher extinction coefficients, and organic solar cells with higher PCE.[29] On the other hand, some of us showed that replacing one of the external phenyl rings of triphenylamine (TPA) in push-pull molecule TPA-T-DCV by a methyl group, directly connected to the nitrogen atom (MPA-T-DCV), led to an improved photovoltaic performance of TPA-T-DCV mainly due to a significant increase in hole-mobility.[30–32]

By combining these two different approaches, we here describe the synthesis and characterization of four novel push-pull molecules (Figure 1). They display a BTZ π-spacer connecting a DCV electron-acceptor block to four different arylamine-based donor blocks. First, a *N*-methyl-*N*-phenylaniline and a *N*-methyl-*N*-thienylaniline have been used leading to push-pull molecules MPA and MTA, respectively, allowing to study the impact of the thiophene ring on the electronic properties. Finally, a methyl group has been introduced at the *para*-position of the external phenyl ring of the donor blocks, resulting in derivatives Me-MPA and Me-MTA, respectively. We have investigated the performance of these push-pull molecules as donor materials with C_{60} as acceptor in OSCs. Using a fully evaporated model system, we have focused on how methylation at the *para*-position of the external phenyl ring of the arylamine donor block affects the V_{oc} of the devices.
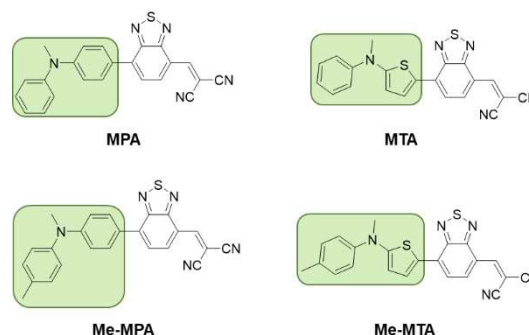

Figure 1. Chemical structures of the novel push-pull D-π-A molecules used in this study. The donor building blocks are highlighted in green.

ChemSusChem

Full Papers
doi.org/10.1002/cssc.202100799

Chemistry Europe
European Chemical
Societies Publishing
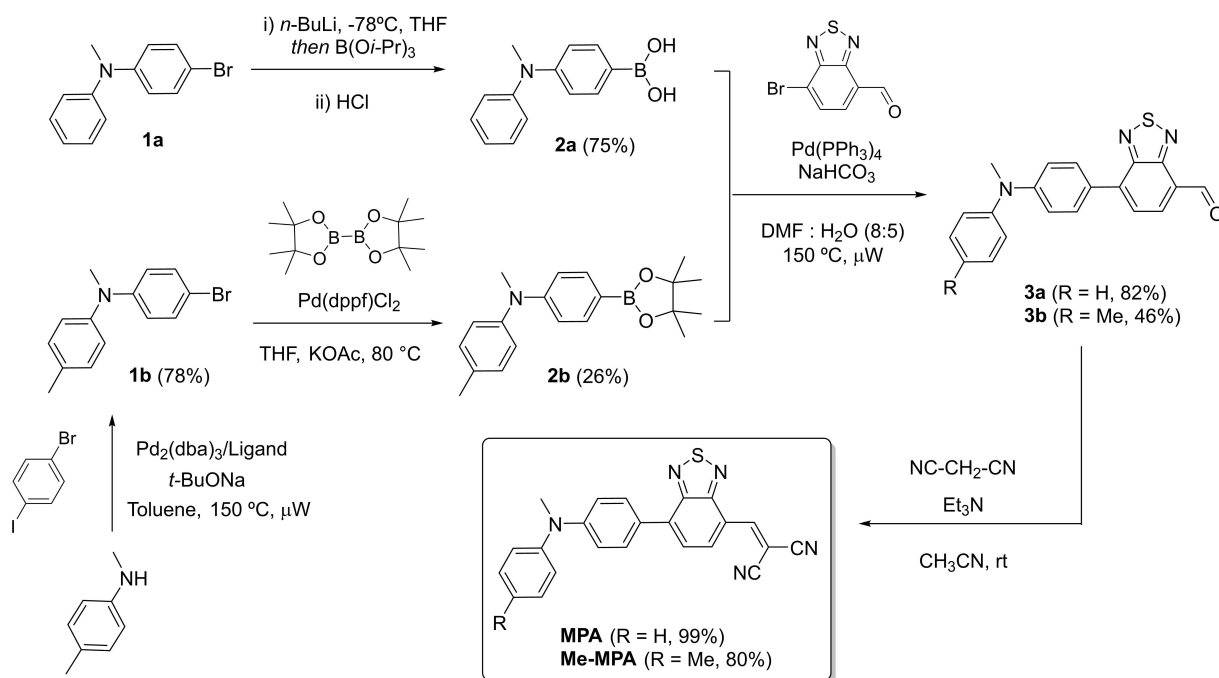
Results and Discussion

Donor synthesis and characterization

The synthesis of the benzenic (MPA) and thiophenic (MTA) push-pull molecules are depicted in Schemes 1 and 2, respectively. 4-Bromo-N-methyl-N-phenylaniline derivatives **1a**[33] and **1b** were transformed into boronic acid (**2a**) and pinacol ester (**2b**), respectively. Compound **1b** was effectively prepared by a Buchwald-Hartwig amination between N,4-dimethylaniline and 1-bromo-4-iodobenzene using [1,1′-biphenyl]-2-yldicyclohexyl-phosphane as ligand. Compounds were then engaged in a Pd-catalyzed cross-coupling reaction with 7-bromobenzo[c][1,2,5]thiadiazole-4-carbaldehyde[34] affording aldehydes **3a** and **3b**. A
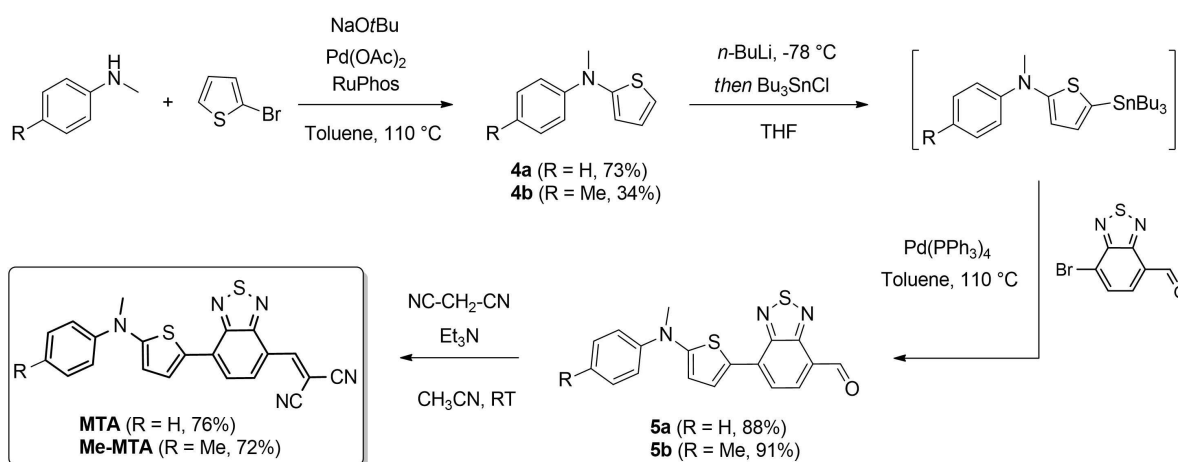
subsequent Knoevenagel condensation with malononitrile led to MPA and Me-MPA (Scheme 1).

Similarly, the two MTA blocks **4a** and **4b**, shown in Scheme 2, were obtained via a Buchwald-Hartwig amination between 2-bromothiophene and N-methylaniline or N,4-dimethylaniline, respectively, using RuPhos as phosphine ligand. After introduction of a tributylstannyl group at the free α-position of thiophene, a Stille coupling with 7-bromobenzo[c][1,2,5]thiadiazole-4-carbaldehyde gave compounds **5**, which were engaged in a Knoevenagel condensation, as described above, to give the compounds MTA and Me-MTA. NMR and mass spectra are shown in Figures S2–S23.

The electrochemical properties of the target molecules were analyzed by cyclic voltammetry (CV) using 0.1 M of Bu_4NPF_6 in

Scheme 1. Synthesis of MPA-derived push-pull molecules.

Scheme 2. Synthesis of MTA-derived push-pull molecules.

These are not the final page numbers! ↗↗

CH_2Cl_2 (see the Supporting Information, Figure S24). All data are summarized in Table S1 and the electrochemical potentials are expressed versus the ferrocene/ferrocenium couple (Fc/Fc$^+$).

As expected for push-pull D-π-A systems, the UV/Vis absorption spectra of the investigated molecules in solution (in CH_2Cl_2) mainly exhibit an intense and broad absorption band in the visible range attributed to an intramolecular charge transfer (ICT) from the donor to the electron-withdrawing moiety (Figure 2). While the MPA derivatives show an ICT band ranging from 450 to 700 nm, the absorption spectra of the thiophenic counterparts are bathochromatically shifted up to 800 nm with absorption maxima around 660 nm. Interestingly, whereas the introduction of methyl groups in Me-MPA and Me-MTA produces a slight redshift of the ICT band ($\approx$ 8–9 nm), it significantly increases their molar extinction coefficients indicating better absorption properties than for MPA and MTA, respectively. UV/Vis absorption of thin films is shown in Figures S25–S28. The highest occupied molecular orbital (HOMO) energy levels of the push-pull molecules were estimated on thin-films from the ionization energy measured by photoelectron spectroscopy in air (PESA, see the Supporting Information, Figures S29–S32). These data are summarized in Table S2.

Device performance

OPV devices were built comprising 30 nm D:A bulk-heterojunction (BHJ) active layer with 1:1 wt% D:C$_{60}$ ratio in the blend. All devices were prepared in a p-i-n (standard) architecture, with 3 nm MoO_3 and 8 nm BPhen as hole- and electron-transporting layers, respectively. From the EQE spectra, shown in Figure 3a, it can be clearly seen that a redshift in the absorption is achieved upon changing the central phenyl ring with a thiophene. As a result, more photons are harvested from the lower-energetic part of the solar spectrum and the short-circuit current density (J_{sc}) is increased, as shown in the current density-voltage (J-V) characteristics in Figure 3b. The photovoltaic fingerprints of the studied devices are summarized in Table 1.

Determination of the optical gap

To investigate voltage losses, E_g^{opt} for each material is determined, setting the upper limit for the V_{oc} when assuming only radiative recombination. Here, we use the definition of E_g^{opt}, as described by Rau et al.,[7] which is directly determined from the measured EQE spectrum of the device. The derivative of the low-energy edge of EQE is interpreted as the distribution of optical gap energies P(E_g), and E_g^{opt} is defined as the mean peak energy of this distribution [Eq. (4)]:

$$E_g^{opt} = \frac{\int_a^b E_g P(E_g) dE_g}{\int_a^b P(E_g) dE_g} \tag{4}$$

where the integration limits a and b are chosen such that P(E_g) is approximately equal to 50% of its maximum value. Since this quantity is calculated from the photovoltaic EQE spectrum, it is
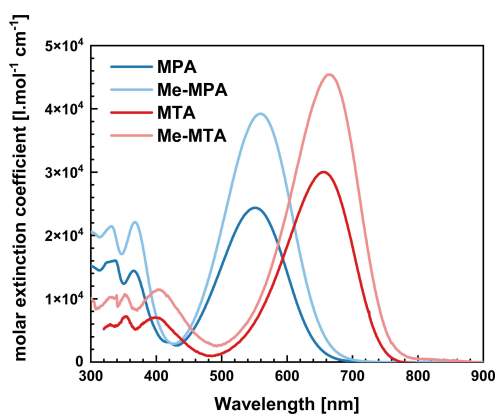

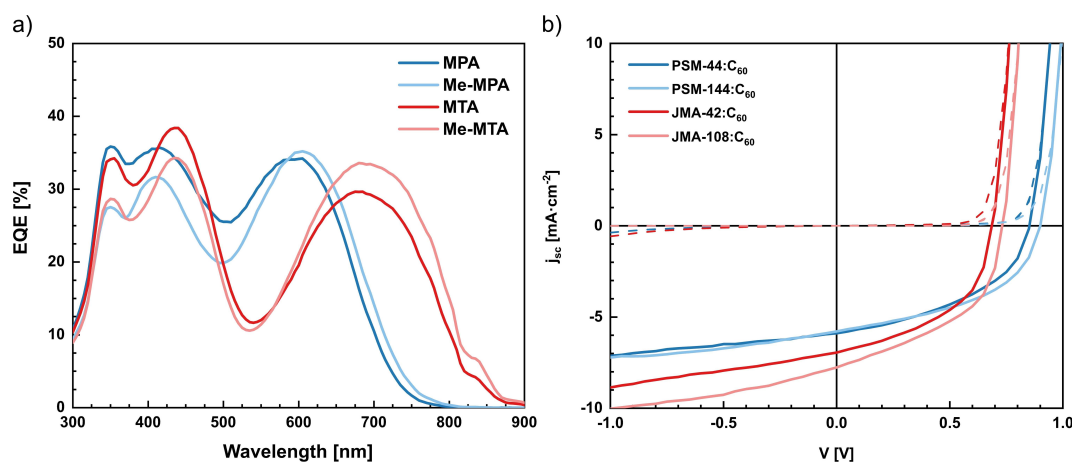**Figure 2.** UV/Vis transmission spectra of investigated compounds in CH_2Cl_2.

Figure 3. (a) EQE spectra and (b) J-V characteristics of the studied devices based on push-pull molecules (solid lines), measured at simulated AM1.5g conditions. The dashed lines represent J-V characteristics measured in the dark.

These are not the final page numbers! ↗↗

ChemSusChem

Full Papers
doi.org/10.1002/cssc.202100799

Chemistry Europe
European Chemical
Societies Publishing

Table 1. Photovoltaic fingerprints of investigated devices (30 nm donor: C_{60}, 1:1 weight ratio).

Device, donor	J_{sc} [mA cm^{-2}]	V_{oc} [V]	FF [%]	E_g^{opt} [eV]
MPA	5.89	0.852	44.8	1.841
Me-MPA	5.79	0.900	47.7	1.810
MTA	6.94	0.686	48.4	1.572
Me-MTA	7.77	0.732	47.1	1.557

therefore directly related to the device performance and is the most suitable choice when investigating voltage losses of the device.[7,35] The calculated E_g^{opt} values for every device are included in Table 1. The overall short-circuit current is only slightly increased due to simultaneous decrease of the absorption in the blue-green region of the spectrum. Replacing the phenyl ring (MPA) with thiophene (MTA) leads to a decrease in the V_{oc}, which is in agreement with higher-energy HOMO levels, as estimated from PESA measurements. On the other hand, the V_{oc} is increased for both methylated donors by roughly 50 mV, which could be explained by (1) decrease of E_{CT} or (2) reduced voltage losses. In the next paragraph, detailed analysis of the energetic landscape and voltage losses are discussed to explain this phenomenon.

Charge-transfer state properties

In OSCs, the CT state is the lowest absorbing and emitting state and therefore its properties have crucial impact on the V_{oc} and overall performance of the device.[8,36] To better understand the energy losses in the studied devices, the low-energy tail of the EQE spectrum is measured sensitively over several orders of magnitude and fitted with Equation (5)[36] to extract CT state properties, as shown in Figure 4. This sensitively measured EQE spectrum will be referred to as EQE$_{PV}$.
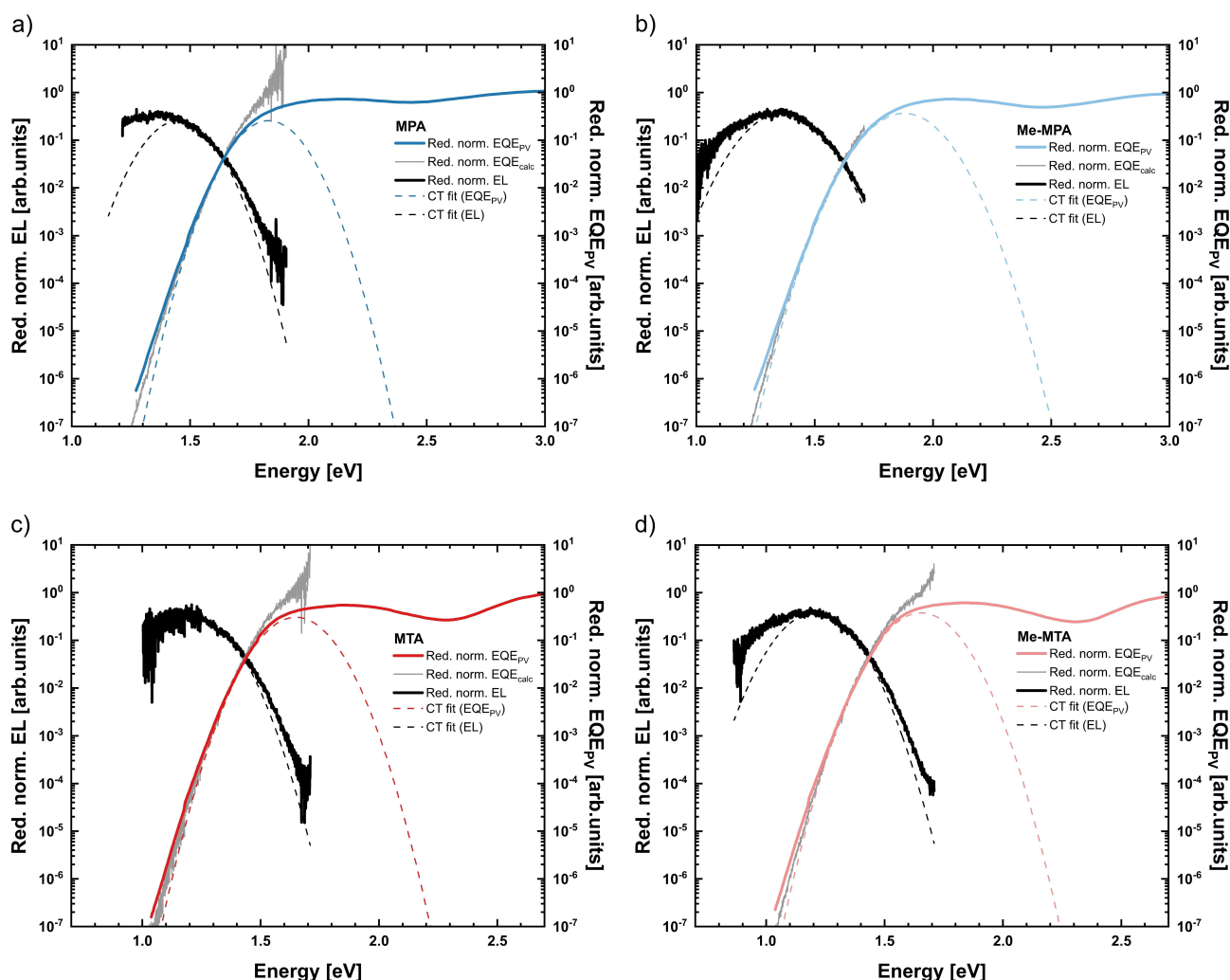

Figure 4. Reduced EQE$_{PV}$ and EL spectra of devices based on (a,b) MPA and Me-MPA and (c,d) MTA and Me-MTA donor molecules, respectively. The dashed lines represent fits to the experimental EQE$_{PV}$ and EL spectra using Equations (5) and (6), respectively. Emission and absorption of the CT state are connected by the reciprocity relation and therefore both spectra can be used to obtain E_{CT} and λ_{CT}. The intersection point of those two curves equals E_{CT}. The grey curve corresponds to the EQE$_{PV}$ calculated from the EL spectra by assuming room temperature for the black-body spectrum. The analysis proves that the spectra are in accordance with the reciprocity relation between emission and absorption.

Table 2. Electronic parameters and corresponding voltage losses for the studied devices.

Device, donor	E_{CT} [eV]	ΔE_{CT} [eV]	V_{rad} [V]	V_{oc} [V]	ΔV_r [V]	ΔV_{nr}[a] [V]	ΔV_{nr}[b] [V]
MPA	1.642	0.199	1.290	0.852	0.352	0.438	0.474
Me-MPA	1.621	0.189	1.272	0.900	0.349	0.372	0.385
MTA	1.435	0.137	1.089	0.686	0.346	0.402	0.436
Me-MTA	1.431	0.126	1.085	0.732	0.346	0.353	0.377

[a] ΔV_{nr} calculated using Equation (7), based on the measured EQE_{PV} spectrum. [b] ΔV_{nr} obtained from the radiative EL quantum yield, calculated using Equation (3).

$$EQE_{PV}(E) \times E = \frac{f}{\sqrt{4\pi k_B T \lambda_{CT}}} \times \exp\left(\frac{-(E+\lambda_{CT}-E)^2}{4k_B T \lambda_{CT}}\right) \quad (5)$$

The product of $EQE_{PV}(E) \times E$ is referred to as reduced EQE_{PV}; f equals $IQE_{PV}N_{CT}2df_\sigma$ (d is the thickness of the light-absorbing layer and f_σ the dipole coupling of the CT state to the ground state). Due to the reciprocity relation between emission and absorption of the CT state,[36] EL spectra can also be used to extract E_{CT} and λ_{CT} [Eq. (6)]:

$$\frac{EL(E)}{E} = \frac{f_I}{\sqrt{4\pi k_B T \lambda_{CT}}} \times \exp\left(\frac{-(E-\lambda_{CT}-E)^2}{4k_B T \lambda_{CT}}\right) \quad (6)$$

Similarly, here the term $EL \times E^{-1}$ is referred to as reduced EL spectrum. It is important to note that both Equations (5) and (6) differ only by the prefactor f and f_I and the sign of λ_{CT}. Setting $f_I = f$ normalizes both reduced spectra such that their crossing point energy is equal to the energy of the CT state. A summary of all obtained electronic parameters is listed in Table S3. It is worth pointing out that E_{CT} for both devices in each pair is similar, especially in the case of devices MTA and Me-MTA, where the energy difference is only 4 meV.

Investigation of the voltage losses

Since E_{CT} is similar, the increase in the V_{oc} for the methylated molecules can be connected to decreased voltage losses. Using E_{CT} extracted from the fits to the EQE_{PV} and EL spectra and E_g^{opt}, we computed the driving force $\Delta E_{CT} = E_g^{opt} - E_{CT}$ to be nearly identical for both devices in each pair. The V_{oc} in the radiative limit, calculated using Equation (2), is also similar. Now, it is possible to quantify the amount of both radiative and non-radiative voltage losses [Eqs. (7) and (8)]:

$$\Delta V_r = \frac{E_{CT}}{q} - V_{rad} \quad (7)$$

$$\Delta V_{nr} = V_{rad} - V_{oc} \quad (8)$$

Electronic parameters of each device and their corresponding voltage losses are presented in Table 2. We find that the radiative limit for the V_{oc} is similar in each pair and the radiative voltage losses change negligibly between the devices. On the other hand, the non-radiative voltage losses are reduced by approx. 50 mV for the devices based on methylated donor

molecules. ΔV_{nr} was obtained using two independent techniques, namely using Equation (7) with measured EQE_{PV} spectrum and directly from the EQE_{EL} measurements (see the Supporting Information, Table S4). Both methods show the same trend of decreasing ΔV_{nr} upon methylation of the donor molecule.

Recombination dynamics

In order to gain further insight into non-radiative voltage losses, we perform transient photovoltage (TPV) decay measurements to study the recombination dynamics. All measurements are conducted within the small perturbation regime. Photovoltage decays are measured under open-circuit conditions, where no external charges flow and all photogenerated charges must eventually recombine within the device. The photovoltage decay is a well establish technique for probing the lifetime of excess charge carriers generated by a laser pulse in an optically biased device.[37,38] In our model system, we compare two sets of devices, each of which is characterized by almost identical optical gap. This implies that the number of photogenerated charge carriers should be equal between devices in each group, ensuring that the photovoltage decay resembles the recombination dynamics. Exponential decay time constants are obtained by fitting measured photovoltage transients with monoexponential decay function (Figure S34) and are subsequently plotted as a function of the V_{oc} (Figure S35), which allows to extract the lifetime τ of free charge carriers, as shown in Figure 5. The lifetimes for each device are obtained from a fit via Equation (9):

$$\tau = \tau_0 \exp(-\beta V_{oc}) \quad (9)$$

where β is related to the temperature T, the diode ideality factor n_{id} and the recombination order m [Eq. (10)]:

$$\beta = \frac{q}{k_B T}\left(\frac{1}{n_{id}} - \frac{1}{m}\right) \quad (10)$$

As a result, the recombination time constant τ_0 for each device can be calculated.[38] The fitting parameters are summarized in Table S5. The decay times of free charge carriers extracted from TPV measurements confirm that the recombination is slower in devices with lower non-radiative voltage losses. The corresponding charge carrier lifetimes are higher by an order of magnitude. Similar values of β for both groups of
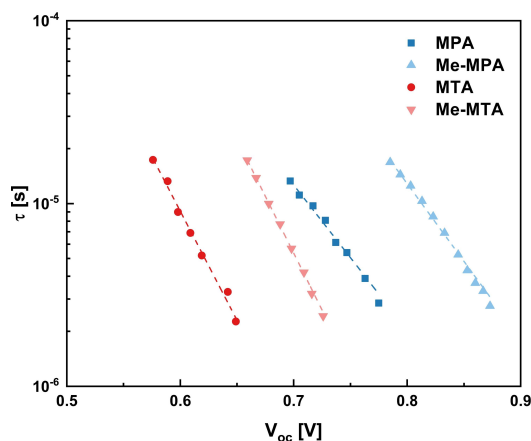
ChemSusChem

Full Papers
doi.org/10.1002/cssc.202100799

**Chemistry
Europe**
European Chemical
Societies Publishing

Figure 5. Lifetimes extracted from the TPV measurements.

Table 3. Energy of the CT state (E_{CT}) and oscillator strength (f) for eight MTA:C_{60} and Me–MTA:C_{60} configurations.

Configuration	MTA:C_{60}		Me-MTA:C_{60}	
	E_{CT} [eV]	f	E_{CT} [eV]	f
1	1.42	0.035	1.40	0.032
2	1.46	0.009	1.51	0.067
3	1.47	0.009	1.50	0.067
4	1.45	0.008	1.51	0.011
5	1.46	0.010	1.53	0.006
6	1.45	0.008	1.45	0.022
7	1.47	0.009	1.52	0.011
8	1.46	0.053	1.45	0.049

devices (see the Supporting Information, Table S5) indicate the same recombination order and diode ideality factors for both devices in each group.[14,38]

According to Azzouzi et al.,[17] there are several molecular parameters that can be responsible for the reduction of non-radiative voltage losses, mostly related to the properties of the CT state at the intermolecular D:A interface. In our set of devices, we can rule out the influence of E_g^{opt} and E_{CT} to be responsible. On the other hand, reorganization energies and the oscillator strength of the transition are still possible parameters accountable for the reduction of ΔV_{nr}.

Computational methods

In order to determine which parameters are the most relevant for reducing non-radiative voltage losses, we perform quantum-chemical calculations at the density functional theory (DFT) level to assess the intramolecular reorganization energy λ upon charging the two donors, MTA and Me-MTA, and the C_{60} acceptor. For the C_{60} molecule, we find a λ^- of 89 meV, while the two donors show similar relaxation energies λ^+ of 137 meV

for MTA and 135 meV for Me-MTA. We then perform time-dependent DFT (TDDFT) calculations on representative D:C_{60} pairs. Namely, as shown in Figure 6, a cluster of C_{60} molecules was built around a single MTA (Me-MTA) donor and each D:C_{60} pair is optimized at the DFT level (see Computational methods for further details).

Full TDDFT calculations were performed on each ground-state optimized molecular configuration in the evaluation of E_{CT} and the oscillator strength f of the first electronic transition. Table 3 summarizes the results obtained for all the MTA:C_{60} and Me-MTA:C_{60} investigated configurations, respectively. We note that the CT state energies coming from TDDFT calculations are corrected by the total reorganization energy $\lambda = \lambda^+ + \lambda^-$.

On average, all the investigated configurations show a similar E_{CT} (1.46 eV for MTA:C_{60} pairs and 1.48 eV for Me-MTA:C_{60} ones) in agreement with experimental data. Most interestingly, we observed a significant increase in oscillator strength in the case of the methylated molecules (the average f value increases from 0.018 in MTA:C_{60} pairs to 0.033 in Me-MTA:C_{60} pairs). It is interesting to have a closer look at configuration entry 2 in Table 3, as this provides the largest difference in oscillator strength between MTA and Me-MTA donors. The corresponding 3D transition dipole density surfaces are plotted in Figure 7.

Figure 7 shows that the presence of the additional methyl group on the aromatic ring tends to bend the molecule over the C_{60} acceptor in order to maximize π-π interactions. This
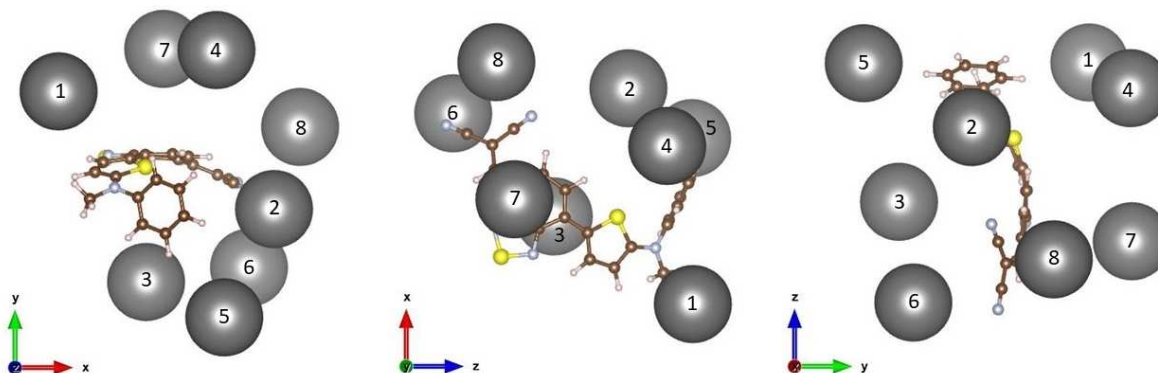

Figure 6. Different representations of the cluster of C_{60} molecules (cue balls in grey) around the MTA donor. Eight different D:C_{60} configurations were chosen for TDDFT calculations.
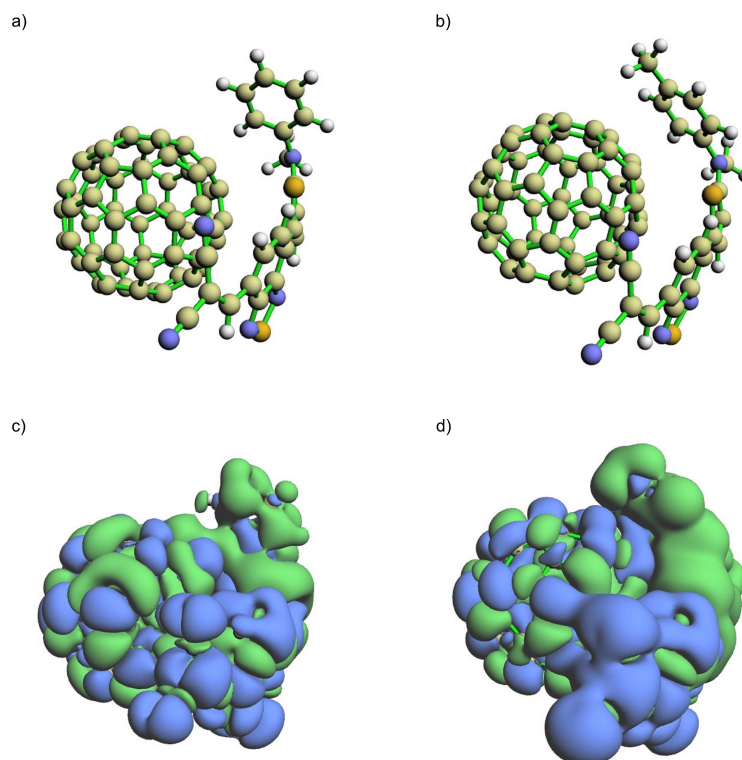
These are not the final page numbers! ↗↗

ChemSusChem

Full Papers
doi.org/10.1002/cssc.202100799

Chemistry Europe
European Chemical
Societies Publishing

Figure 7. (a, b) Optimized D : A structures (configuration no. 2) and (c, d) positive (green) and negative (blue) part of the transition dipole density surfaces for MTA : C_{60} and Me–MTA : C_{60}, respectively.

results in a more intimate interaction of the donor molecule with C_{60} that translates into a slightly larger contribution from the aromatic amine moiety of the donor to the transition density (seen as the green isosurface in Figure 7). The larger wave function overlap manifested by the transition density distribution turns into a larger oscillator strength and, according to the model proposed by Azzouzi et al.,[17] accounts for reduced non-radiative voltage losses in OPV devices based on methylated versions of the molecular donors.

Conclusion

We study a model system based on novel push-pull, donor-π-acceptor molecules, used as donors in organic solar cells (OSCs) with C_{60} as acceptor. We find that adding methyl groups to the donor molecule increases the open-circuit voltage (V_{oc}) of the device. Utilizing highly sensitive measurement techniques, we analyze the properties of the charge-transfer state within the devices and calculate the corresponding voltage losses. While the amount of radiative voltage losses remains unaffected by the modification of the donor, the non-radiative voltage losses are reduced by about 50 mV. Studies of the transient photo-voltage decays reveal that for methylated molecules, the recombination rate is slower. From quantum-chemical calculations, we find that main reason for the reduction of non-radiative voltage losses is an increase in the oscillator strength of the electronic transition, associated with a more intimate

interaction at the molecular scale between donor and acceptor molecules.

Experimental Section

UV/Vis

UV/Vis spectra were recorded in dichloromethane or as thin-films on indium tin oxide (ITO) substrates using a PERKIN ELMER 950 spectrometer.

Cyclic voltammetry

CV was performed using a BIOLOGIC SP-150 potentiostat with positive feedback compensation in 0.10 M Bu$_4$NPF$_6$/CH$_2$Cl$_2$ (HPLC grade). Experiments were carried out in a one-compartment cell equipped with a platinum working electrode (2 mm diameter) and a platinum wire counter electrode. A silver wire immersed in a 0.01 M solution of AgNO$_3$ in CH$_3$CN was used as reference electrode and checked against the ferrocene/ferrocenium couple (Fc/Fc$^+$) before and after each experiment. The potentials were then expressed vs. Fc/Fc$^+$.

Photoelectron spectroscopy in air

PESA measurements were recorded using a Riken Keiki PESA spectrometer (Model AC-2); samples were spin-cast over ITO substrates and irradiated with a laser beam with power settings of approximately 20 nW; the electron detector allows to measure the ionization potential operating in atmospheric air.

© 2021 The Authors. ChemSusChem published by Wiley-VCH GmbH

These are not the final page numbers! ⌐⌐

Device preparation

Devices were prepared by vacuum thermal evaporation in a high-vacuum system with a base pressure of $< 10^{-7}$ mbar (Kurt J. Lesker Ltd.). All layers of materials were evaporated onto a glass substrate with a pre-structured ITO contact (Thin Film devices), cleaned in subsequent ultrasonic baths with *N*-methyl-2-pyrrolidone, deionized water, and ethanol and ultraviolet ozone cleaning system. Prior to evaporation, all organic materials were purified by vacuum gradient sublimation. Metal contacts were deposited through a shadow mask, to form a top contact and overlap with the bottom ITO contact, thus defining the device area of 6.44 mm². To avoid degradation due to external conditions, all devices were encapsulated with a glass cavity glued on the substrate together with a moisture getter.

All provided materials were tested as donors against C_{60} fullerene acceptor (CreaPhys GmbH), incorporated in a p-i-n (standard) device architecture, using molybdenum oxide (MoO_3) (Sigma Aldrich) and bathophenanthroline (BPhen) (Lumtec), as hole- and electron-transporting layers (HTL and ETL), respectively. The structure of a complete device is:

ITO/MoO_3 (3)/BHJ (30, 1 : 1 wt%)/C_{60} (15)/BPhen (8)/Ag(100)

Numbers in brackets represent the thicknesses in nm of the respective layer.

Current-voltage characteristics

Current density-voltage (*J-V*) characteristics were measured with a source-measurement unit (Keithley 2400, Keithley Ltd.). The sample was illuminated by a sun simulator (16S-150V.3, Solar Light Co.) with intensity adjusted such as to generate the current corresponding to an AM1.5g spectrum (100 mW cm⁻²), calibrated with silicon photodiode (S1337, Hamamatsu, calibrated by Fraunhofer ISE).

External quantum efficiency spectra

EQE spectra were measured using light from a xenon lamp (Apex 150 W Xenon Arc Lamp, Newport Oriel) and a monochromator (Cornerstone 260 1/4m, Newport Oriel). Signal from the device was pre-amplified and recorded with a lock-in amplifier (SR 7265 Lock-In amplifier, Signal Recovery) with 0.2 s time constant. The reference spectrum was taken with a silicon reference diode (S1337, Hamamatsu, calibrated by Fraunhofer ISE).

Sensitive EQE_PV measurements

To measure the sensitive EQE_{PV} spectra, light from the 50 W halogen lamp was chopped at 143 Hz and fed into the monochromator (Cornerstone 260 1/4m, Newport Oriel). The output beam was focused onto the OSC under short-circuit condition. Current from the solar cell was pre-amplified and analyzed with lock-in amplifier (Signal Recovery, 7280 DSP), coupled with the chopper. Time constant of the lock-in was set in the range of 0.5–2.0 s in order to resolve low-current signals and the pre-amplification was set accordingly. Final spectra were calculated by dividing the obtained photocurrent by incident photon flux, measured with calibrated silicon and indium gallium arsenide photodiodes.

Transient photovoltage measurements

TPV decays were obtained by connecting the OSC to a high-impedance (1 MΩ) input of the digital oscilloscope (DPO7354C, Tektronix Inc.). The V_{oc} of the device was adjusted with a bias light, produced by a high-power LED (LED Engin, Osram Inc.), controlled by an external power supply (EA-PS 3032-10B, EA Elektro-Automatik GmbH). An additional light pulse, generated by picosecond Nd:YAG laser (PL2210, Ekspla), was focused on the device and disturbed the steady state, creating a voltage spike, whose decay was measured at the oscilloscope.

Electroluminescence

Relative electroluminescence spectra were recorded by liquid N₂-cooled InGaAs- and silicon-CCD-cameras (Princeton Instruments PyLoN:IR and Spec-10:100) on the exit slit of a 500 mm spectrograph (Princeton Instruments Acton 500i). Both cameras were calibrated prior to the experiment using a quart-tungsten-halogen irradiance standard. A source-measure-unit (Keithley 2634B) was used to apply constant forward driving currents to the OSC. All spectra were recorded multiple times while driving currents were varied over 2 orders of magnitude to exclude heating effects or additional emission pathways.

Electroluminescence quantum yield

Absolute radiative quantum yields were determined by placing a 1 cm² large silicon photodiode (Thorlabs FDS1010) in close proximity (≈3 mm) to the solar cells emissive area. While the solar cell was held at a constant bias voltage (with the injection current measured by a Keithley 2000 DMM), the diode's photocurrent was measured with a Keithley 480 Picoammeter. The emission yield was then calculated from the photocurrent and the spectral overlap between the photodiode's EQE and the solar cell's electroluminescence spectrum, and includes a geometric mismatch factor based on the assumed Lambertian emission profile and reflection at the metal back electrodes.

Computational methods

The effect of intramolecular structural relaxation upon charging was considered by calculating the intramolecular reorganization energy of an isolated C_{60}, MTA, and Me-MTA molecule. Specifically, as described elsewhere,[39,40] the intramolecular reorganization energy λ^q, averaged on the charging and discharging processes, was computed as follows [Eq. (11)]:

$$\lambda^q = \frac{\left|E^q(R_0) - E^q(R_q)\right| + \left|E^0(R_q) - E^0(R_0)\right|}{2} \quad (11)$$

where q stands for the charge on the molecule and R_0 and R_q indicate the equilibrium geometries of neutral and charged states. Geometries were optimized using a range-separated hybrid functional as ωB97X-D,[41] along with the 6-31g(d) basis set, keeping the donors molecular soft degrees of freedom (dihedral angles) frozen, as to account only for the contribution from high-frequency modes, as described elsewhere.[39,40] Donor:C_{60} pairs were optimized at the ground-state DFT level using the same level of theory as described above. Energies of the CT state and oscillator strengths were computed with TDDFT calculations employing the same functional and the 6-31g(d,p) basis set. In addition, the range-separation parameter ω was optimally tuned in the presence of a polarizable continuum model (PCM)[42] setting the macroscopic dielectric

constant at $\varepsilon = 3.00$. DFT and TDDFT calculations were carried out with Gaussian16 software.[43]

Acknowledgements

Conflict of Interest

The authors declare no conflict of interest.

[1] Q. Liu, Y. Jiang, K. Jin, J. Qin, J. Xu, W. Li, J. Xiong, J. Liu, Z. Xiao, K. Sun, S. Yang, X. Zhang, L. Ding, *Sci. Bull.* **2020**, *65*, 272–275.

[2] W. Zhao, S. Li, H. Yao, S. Zhang, Y. Zhang, B. Yang, J. Hou, *J. Am. Chem. Soc.* **2017**, *139*, 7148–7151.

[3] Z. Zheng, Q. Hu, S. Zhang, D. Zhang, J. Wang, S. Xie, R. Wang, Y. Qin, W. Li, L. Hong, N. Liang, F. Liu, Y. Zhang, Z. Wei, Z. Tang, T. P. Russell, J. Hou, H. Zhou, *Adv. Mater.* **2018**, *30*, 1801801.

[4] M. Jeong, I. W. Choi, E. M. Go, Y. Cho, M. Kim, B. Lee, S. Jeong, Y. Jo, H. W. Choi, J. Lee, J.-H. Bae, S. K. Kwak, D. S. Kim, C. Yang, *Science* **2020**, *369*, 1615–1620.

[5] M. Riede, D. Spoltore, K. Leo, *Adv. Energy Mater.* **2021**, *11*, 2002653.

[6] K Vandewal, J. Benduhn, V. C. Nikolis, *Sustain. Energy Fuels* **2018**, *7*.

[7] U. Rau, B. Blank, T. C. M. Müller, T. Kirchartz, *Phys. Rev. Applied* **2017**, *7*, 044016.

[8] K. Vandewal, *Annu. Rev. Phys. Chem.* **2016**, *67*, 113–133.

[9] A. Classen, C. L. Chochos, L. Lüer, V. G. Gregoriou, J. Wortmann, A. Osvet, K. Forberich, I. McCulloch, T. Heumüller, C. J. Brabec, *Nat. Energy* **2020**, *5*, 711–719.

[10] J. Liu, S. Chen, D. Qian, B. Gautam, G. Yang, J. Zhao, J. Bergqvist, F. Zhang, W. Ma, H. Ade, O. Inganäs, K. Gundogdu, F. Gao, H. Yan, *Nat. Energy* **2016**, *1*, 16089.

[11] V. C. Nikolis, J. Benduhn, F. Holzmueller, F. Piersimoni, M. Lau, O. Zeika, D. Neher, C. Koerner, D. Spoltore, K. Vandewal, *Adv. Energy Mater.* **2017**, *7*, 1700855.

[12] W. Shockley, H. J. Queisser, *J. Appl. Phys.* **1961**, *32*, 510–519.

[13] P. Würfel, U. Würfel, *Physics of Solar Cells*: From Basic Principles to Advanced Concepts, Wiley, **2016**.

[14] K. Vandewal, J. Widmer, T. Heumueller, C. J. Brabec, M. D. McGehee, K. Leo, M. Riede, A. Salleo, *Adv. Mater.* **2014**, *26*, 3839–3843.

[15] M. Panhans, S. Hutsch, J. Benduhn, K. S. Schellhammer, V. C. Nikolis, T. Vangerven, K. Vandewal, F. Ortmann, *Nat. Commun.* **2020**, *11*, 1488.

[16] J. Benduhn, K. Tvingstedt, F. Piersimoni, S. Ullrich, Y. Fan, M. Tropiano, K. A. McGarry, O. Zeika, M. K. Riede, C. J. Douglas, S. Barlow, S. R. Marder, D. Neher, D. Spoltore, K. Vandewal, *Nat. Energy* **2017**, *2*, 17053.

[17] M. Azzouzi, J. Yan, T. Kirchartz, K. Liu, J. Wang, H. Wu, J. Nelson, *Phys. Rev. X* **2018**, *8*, 031055.

[18] A. Mishra, P. Bäuerle, *Angew. Chem. Int. Ed.* **2012**, *51*, 2020–2067; *Angew. Chem.* **2012**, *124*, 2060–2109.

[19] A. Venkateswararao, K.-T. Wong, *Bull. Chem. Soc. Jpn.* **2021**, *94*, 812–838.

[20] J. Roncali, *Acc. Chem. Res.* **2009**, *42*, 1719–1730.

[21] F. Würthner, K. Meerholz, *Chem. Eur. J.* **2010**, *16*, 9366–9373.

[22] J. Roncali, P. Leriche, P. Blanchard, *Adv. Mater.* **2014**, *26*, 3821–3838.

[23] V. Malytskyi, J.-J. Simon, L. Patrone, J.-M. Raimundo, *RSC Adv.* **2014**, *5*, 354–397.

[24] P. Blanchard, C. Malacrida, C. Cabanetos, J. Roncali, S. Ludwigs, *Polym. Int.* **2019**, *68*, 589–606.

[25] C. Cabanetos, P. Blanchard, J. Roncali, *Chem. Rec.* **2019**, *19*, 1123–1130.

[26] L.-Y. Lin, Y.-H. Chen, Z.-Y. Huang, H.-W. Lin, S.-H. Chou, F. Lin, C.-W. Chen, Y.-H. Liu, K.-T. Wong, *J. Am. Chem. Soc.* **2011**, *133*, 15822–15825.

[27] H.-S. Shim, C.-K. Moon, J. Kim, C.-K. Wang, B. Sim, F. Lin, K.-T. Wong, Y. Seo, J.-J. Kim, *ACS Appl. Mater. Interfaces* **2016**, *8*, 1214–1219.

[28] X. Che, Y. Li, Y. Qu, S. R. Forrest, *Nat. Energy* **2018**, *3*, 422–427.

[29] Y.-H. Chen, L.-Y. Lin, C.-W. Lu, F. Lin, Z.-Y. Huang, H.-W. Lin, P.-H. Wang, Y.-H. Liu, K.-T. Wong, J. Wen, D. J. Miller, S. B. Darling, *J. Am. Chem. Soc.* **2012**, *134*, 13616–13623.

[30] A. Leliège, C.-H. L. Régent, M. Allain, P. Blanchard, J. Roncali, *Chem. Commun.* **2012**, *48*, 8907–8909.

[31] J. W. Choi, C.-H. Kim, J. Pison, A. Oyedele, D. Tondelier, A. Leliège, E. Kirchner, P. Blanchard, J. Roncali, B. Geffroy, *RSC Adv.* **2014**, *4*, 5236–5242.

[32] Y. Jiang, C. Cabanetos, M. Allain, P. Liu, J. Roncali, *J. Mater. Chem. C* **2015**, *3*, 5145–5151.

[33] M. D. Charles, P. Schultz, S. L. Buchwald, *Org. Lett.* **2005**, *7*, 3965–3968.

[34] S. Holliday, R. S. Ashraf, C. B. Nielsen, M. Kirkus, J. A. Röhr, C.-H. Tan, E. Collado-Fregoso, A.-C. Knall, J. R. Durrant, J. Nelson, I. McCulloch, *J. Am. Chem. Soc.* **2015**, *137*, 898–904.

[35] Y. Wang, D. Qian, Y. Cui, H. Zhang, J. Hou, K. Vandewal, T. Kirchartz, F. Gao, *Adv. Energy Mater.* **2018**, *8*, 1801352.

[36] K. Vandewal, K. Tvingstedt, A. Gadisa, O. Inganäs, J. V. Manca, *Phys. Rev. B* **2010**, *81*, 125204.

[37] C. G. Shuttle, B. O'Regan, A. M. Ballantyne, J. Nelson, D. D. C. Bradley, J. de Mello, J. R. Durrant, *Appl. Phys. Lett.* **2008**, *92*, 093311.

[38] O. J. Sandberg, K. Tvingstedt, P. Meredith, A. Armin, *J. Phys. Chem. C* **2019**, *123*, 14261–14271.

[39] A. Privitera, G. Londi, M. Riede, G. D'Avino, D. Beljonne, *Adv. Funct. Mater.* **2020**, *30*, 2004600.

[40] G. Londi, S.-U.-Z. Khan, L. Muccioli, G. D'Avino, B. P. Rand, D. Beljonne, *J. Phys. Chem. Lett.* **2020**, *11*, 10219–10226.

[41] J.-D. Chai, M. Head-Gordon, *Phys. Chem. Chem. Phys.* **2008**, *10*, 6615–6620.

[42] J. Tomasi, B. Mennucci, R. Cammi, *Chem. Rev.* **2005**, *105*, 2999–3094.

[43] M. J. Frisch, G. W. Trucks, H. B. Schlegel, G. E. Scuseria, M. A. Robb, J. R. Cheeseman, G. Scalmani, V. Barone, G. A. Petersson, H. Nakatsuji, X. Li, M. Caricato, A. V. Marenich, J. Bloino, B. G. Janesko, R. Gomperts, B. Mennucci, H. P. Hratchian, J. V. Ortiz, A. F. Izmaylov, J. L. Sonnenberg, Williams, F. Ding, F. Lipparini, F. Egidi, J. Goings, B. Peng, A. Petrone, T. Henderson, D. Ranasinghe, V. G. Zakrzewski, J. Gao, N. Rega, G. Zheng, W. Liang, M. Hada, M. Ehara, K. Toyota, R. Fukuda, J. Hasegawa, M. Ishida, T. Nakajima, Y. Honda, O. Kitao, H. Nakai, T. Vreven, K. Throssell, J. A. Montgomery Jr., J. E. Peralta, F. Ogliaro, M. J. Bearpark, J. J. Heyd, E. N. Brothers, K. N. Kudin, V. N. Staroverov, T. A. Keith, R. Kobayashi, J. Normand, K. Raghavachari, A. P. Rendell, J. C. Burant, S. S. Iyengar, J. Tomasi, M. Cossi, J. M. Millam, M. Klene, C. Adamo, R. Cammi, J. W. Ochterski, R. L. Martin, K. Morokuma, O. Farkas, J. B. Foresman, D. J. Fox, *Gaussian 16 Rev.* C.01, Wallingford, CT, **2016**.

[44] R. W. Friesen, E. M. D. Allouche in *Encyclopedia of Reagents for Organic Synthesis*, American Cancer Society, **2017**, pp. 1–7.

[45] S. S. Zalesskiy, V. P. Ananikov, *Organometallics* **2012**, *31*, 2302–2309.

[46] A. Wilke, J. Endres, U. Hörmann, J. Niederhausen, R. Schlesinger, J. Frisch, P. Amsalem, J. Wagner, M. Gruber, A. Opitz, A. Vollmer, W. Brütting, A. Kahn, N. Koch, *Appl. Phys. Lett.* **2012**, *101*, 233301.
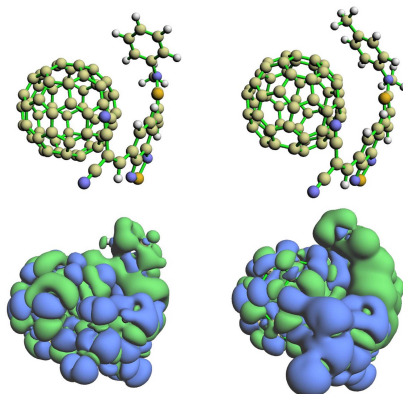
FULL PAPERS

Structural tuning improves efficiency: Modification of the molecular structure of organic molecules allows to influence the performance of organic photovoltaic devices. Addition of a methyl group in the *para*-position of the external phenyl ring leads to increase in open-circuit voltage. Quantum-chemical calculations attribute this effect to the increase of the oscillator strength of the electronic transition between the donor and acceptor.

L. Baisinger*, Dr. J. M. Andrés Castán, Dr. P. Simón Marqués, Dr. G. Londi, C. Göhler, Prof. Dr. C. Deibel, Prof. Dr. D. Beljonne, Dr. C. Cabanetos, Dr. P. Blanchard, Dr. J. Benduhn, Dr. D. Spoltore, Prof. Dr. K. Leo*

1 – 11

Reducing Non-Radiative Voltage Losses by Methylation of Push–Pull Molecular Donors in Organic Solar Cells